Structure
Article

Structural Dynamics of Light-Driven Proton Pumps

Magnus Andersson,[1,5] Erik Malmerberg,[2,5] Sebastian Westenhoff,[2] Gergely Katona,[2] Marco Cammarata,[3] Annemarie B. Wöhri,[1] Linda C. Johansson,[2] Friederike Ewald,[3] Mattias Eklund,[4] Michael Wulff,[3] Jan Davidsson,[4] and Richard Neutze[2,*]

[1]Department of Chemical and Biological Engineering, Chalmers University of Technology, Box 462, SE-40530 Göteborg, Sweden
[2]Department of Chemistry, Biochemistry and Biophysics, University of Gothenburg, Box 462, SE-40530 Göteborg, Sweden
[3]European Synchrotron Radiation Facility, BP 220, Grenoble Cedex 38043, France
[4]Department of Photochemistry and Molecular Science, Uppsala University, Box 523, SE-75120 Uppsala, Sweden
[5]These authors contributed equally to this work
*Correspondence: richard.neutze@chem.gu.se
DOI 10.1016/j.str.2009.07.007

SUMMARY

Bacteriorhodopsin and proteorhodopsin are simple heptahelical proton pumps containing a retinal chromophore covalently bound to helix G via a protonated Schiff base. Following the absorption of a photon, all-*trans* retinal is isomerized to a 13-*cis* conformation, initiating a sequence of conformational changes driving vectorial proton transport. In this study we apply time-resolved wide-angle X-ray scattering to visualize in real time the helical motions associated with proton pumping by bacteriorhodopsin and proteorhodopsin. Our results establish that three conformational states are required to describe their photocycles. Significant motions of the cytoplasmic half of helix F and the extracellular half of helix C are observed prior to the primary proton transfer event, which increase in amplitude following proton transfer. These results both simplify the structural description to emerge from intermediate trapping studies of bacteriorhodopsin and reveal shared dynamical principles for proton pumping.

INTRODUCTION

Although it has long been known that bacteriorhodopsin (Oesterhelt and Stoeckenius, 1971) functions as a light driven proton pump in certain halophilic archaea, it was not until the discovery of the bacterial homolog proteorhodopsin in seawater (Beja et al., 2000) that the pervasive role of bacterial rhodopsins in supplying energy to marine ecosystems was appreciated (Beja et al., 2000, 2001). Subsequent studies have established that light has a positive effect on growth for proteorhodopsin-containing marine bacteria (Gomez-Consarnau et al., 2007) and genetically diverse proteorhodopsin-containing bacteria are distributed throughout the world's oceans (Beja et al., 2001). Moreover, rhodopsin family members also transport ions (Kolbe et al., 2000), serve as light gated channels (Nagel et al., 2002), and harvest the information content of light through animal vision (Palczewski et al., 2000) and archaeal phototaxis (Royant et al., 2001). This genetic and functional diversity implies that nature has utilized common structural and functional principles to fulfill diverse functions across all kingdoms of life.

Bacteriorhodopsin is the best characterized of the rhodopsins. Its remarkable stability has made it a work-horse for understanding the fundamental ingredients of proton pumping in bioenergetics as well as providing a robust prototype for validating new biophysical approaches. Combined spectroscopic and mutational studies (Haupts et al., 1999) have identified the key residues involved in proton pumping (see Figure S1A available online) and early insight into the structure of bacteriorhodopsin was provided by electron diffraction (Henderson et al., 1990; Henderson and Unwin, 1975). Following the advent of membrane protein crystallization in lipidic cubic phases (Landau and Rosenbusch, 1996), X-ray structures of bacteriorhodopsin below 2.0 Å resolution were soon reported (Belrhali et al., 1999; Luecke et al., 1999b). These crystals facilitated 3D intermediate trapping studies performed by illuminating crystals at low temperature (Edman et al., 1999; Royant et al., 2000) or during thawing (Luecke et al., 1999a, 2000; Sass et al., 2000), with X-ray diffraction data collected at cryogenic temperatures. In combination with an electron diffraction structure of a bacteriorhodopsin triple mutant believed to mimic a late photocycle conformation (Subramaniam and Henderson, 2000), a consistent high-resolution structural picture of its mechanism of vectorial proton transport by bacteriorhodopsin emerged (Kuhlbrandt, 2000; Neutze et al., 2002).

Despite the intuitive understanding that resulted from these first intermediate trapping studies, this structural mechanism has not been without controversy. First and foremost, there are now three reported structures pertaining to the bacteriorhodopsin K intermediate (Edman et al., 1999; Matsui et al., 2002; Schobert et al., 2002), five of the L intermediate (Edman et al., 2004; Kouyama et al., 2004; Lanyi and Schobert, 2003, 2007; Royant et al., 2000), eight of the M intermediate (Facciotti et al., 2001; Lanyi and Schobert, 2002, 2006; Luecke et al., 1999a, 2000; Sass et al., 2000; Schobert et al., 2003; Takeda et al., 2004), one of the N intermediate (Schobert et al., 2003), as well as resting-state mutant analogs of the M (Subramaniam and Henderson, 2000) and O (Rouhani et al., 2001) intermediates. Significant movements of the cytoplasmic portions of helices F and G and an extracellular movement of helix C are the most reproducible conformational changes observed in these studies (Table 1). Nevertheless, there is little agreement regarding the magnitude of these movements and different structures can differ significantly in detail (Hirai and Subramaniam, 2009). Moreover, although several structures show similar rearrangements of the extended network of water mediated

Table 1. Summary of Helix Movements Observed in Intermediate Trapping and Mutational Studies of Bacteriorhodopsin and the R Factors Calculated Against Time-Resolved WAXS Difference Data

		PDB		Helix[d]								R[e]	
	Reference	Int.	Gnd.	A	B	C_{EC}	C_{CP}	D	E_{CP}	F_{CP}	G_{CP}	Int.	Late
K-state	(Schobert et al., 2002)	1m0k	1m0k	0.00	0.00	0.00	0.00	0.00	0.00	0.00	0.01	1.00[a]	0.96[a]
	(Edman et al. 1999)	1qko	1qkp	0.02	0.02	0.12	0.01	0.01	0.01	0.01	0.12	1.00[a]	0.96[a]
	(Matsui et al., 2002)	1ixf	1iw6	0.12	0.07	0.09	0.06	0.09	0.08	0.07	0.06	0.75	0.92
L-state	(Lanyi and Schobert, 2007)	2ntw	2ntu	0.09	0.08	0.11	0.09	0.07	0.06	0.10	0.13	1.00[a]	0.93
	(Kouyama et al., 2004)	1ucq	1iw6	0.20	0.23	0.18	0.13	0.16	0.14	0.17	0.23	0.98	0.88
	(Lanyi and Schobert, 2003)	1o0a	1o0a	0.12	0.29	0.30	0.29	0.32	0.18	0.38	0.32	1.00[a]	0.96[a]
	(Royant et al., 2000)	1e0p	1e0p	0.36	0.26	0.54	0.28	0.30	0.23	0.44	0.42	0.76	0.86
	(Edman et al., 2004)	1vjm	1vjm	0.37	0.40	0.59	0.47	0.37	0.48	0.61	0.50	0.68	0.81
	Intermediate state			0.00	0.00	1.00	0.09	0.00	0.31	2.23	0.22	**0.34**	-
M-state	(Schobert et al. 2003)	1ph8	1ph8	0.13	0.24	0.25	0.26	0.24	0.26	0.36	0.29	0.91	0.96[a]
	(Lanyi and Schobert, 2006)[b]	2i20	2i1x	0.23	0.19	0.30	0.25	0.19	0.18	0.38	0.39	1.00[a]	0.96[a]
	(Takeda et al., 2004)	1iw9	1iw6	0.22	0.39	0.39	0.14	0.20	0.21	0.30	0.48	1.00[a]	0.96[a]
	(Facciotti et al., 2001)	1kg8	1kgb	0.26	0.23	0.38	0.28	0.28	0.23	0.42	0.38	1.00[a]	0.96[a]
	(Luecke et al., 2000)	1f4z	1f50	0.32	0.28	0.36	0.38	0.21	0.34	0.44	0.41	0.94	0.92
	(Lanyi and Schobert, 2002)	1m0m	1m0m	0.44	0.46	0.59	0.42	0.41	0.31	0.66	0.66	0.96	0.96[a]
	(Luecke et al., 1999a)[b]	1c8s	1c8r	0.28	0.38	0.38	1.04	0.39	0.38	0.91	0.49	0.75	0.70
	(Sass et al., 2000)	1cwq	1cwq	0.52	0.57	0.77	0.56	0.50	0.40	0.90	0.82	0.98	0.96
	(Subramaniam and Henderson, 2000)[c]	1fbk	1fbb	0.40	0.55	0.32	0.51	0.39	0.61	1.84	1.05	0.69	0.82
	Late state			0.00	0.00	1.54	0.13	0.00	0.45	2.92	0.22	-	**0.25**
N	(Schobert et al., 2003)[b]	1p8u	1p8u	0.27	0.49	0.56	0.54	0.49	0.40	0.65	0.66	0.77	0.80
O-state	(Rouhani et al., 2001)[c]	1jv7	1brx	0.71	0.86	1.00	0.49	1.19	0.56	0.50	0.57	0.68	0.54
	R(Rouhani et al., 2001)[c]	1jv6	1brx	0.54	0.90	1.13	0.55	1.16	0.59	0.50	0.53	0.92	0.66
pR	**Late state**			0.00	0.00	0.87	0.00	0.00	0.77	2.62	1.17	-	**0.28**

Yellow indicates that the movement is larger than the average listed movement; orange indicates that the movement is larger than the average listed movement plus one standard deviation.

[a]No positive correlation between predicted difference WAXS curve and experiment (i.e., the predicted curve was multiplied by zero in recovering the optimal R factor).

[b]Illuminated bR mutant.

[c]Nonilluminated bR mutant intermediate state analog.

[d]For bR, the sampled helical movements are defined for the following residue numbers: A, 9–29; B, 36–63; C_{EC}, 79–89; C_{CP}, 90–101; D, 104–126; E_{CP}, 143–153; F_{CP}, 168–186; G, 200–225. The cytoplasmic boundaries for helices E and F were chosen to avoid some very significant variations in this loop. The corresponding residues for pR were: A, 29–49; B, 55–82; C_{EC}, 91–101; C_{CP}, 102–113; D, 120–142; E_{CP}, 157–167; F_{CP}, 183–201; G_{CP}, 215–240. The numbers given in the table are the root mean square displacement on C_α atoms.

[e]R values for the late and intermediate states were calculated against the corresponding time-resolved wide-angle X-ray scattering basis spectra as *R factor* = $\sum\sqrt{(\Delta S^{theory} - \Delta S^{expt})^2} / \sum\sqrt{(\Delta S^{expt})^2}$. In several cases it was necessary to remove some residues from the models in order to make the residues in the resting and intermediate state conformations match.

H-bond interactions, which characterize the extracellular proton-transport pathway (Figure S2), there has been debate concerning when in the photocycle these chemically important structural changes occur. Some structures (Edman et al., 2004; Royant et al., 2000), but not all (Kouyama et al., 2004; Lanyi and Schobert, 2003, 2007), show this H-bond network to have reorganized already by the L intermediate (Figure S2), whereas most structures (Facciotti et al., 2001; Luecke et al., 1999a, 2000; Sass et al., 2000; Schobert et al., 2003; Takeda et al., 2004), but again not all (Lanyi and Schobert, 2002, 2003), show such movements in the M intermediate. The timing of the primary proton transfer event (the L-to-M transition) relative to these structural perturbations is the key when distinguishing between two structural mechanisms proposed for proton pumping by bacteriorhodopsin, where it has been argued that these H-bond changes are essential to set the chemical stage for proton transfer (Edman et al., 2004; Neutze et al., 2002; Royant et al., 2000), whereas the opposing view is that they are a consequence (Lanyi and Schobert, 2003; Luecke et al., 2000), but not a cause, of proton transfer.

Other experimental approaches are therefore essential in order to identify the most significant helical motions in the photocycle of bacteriorhodopsin and when they occur. At first glance, projection difference maps recovered from 2D crystals of

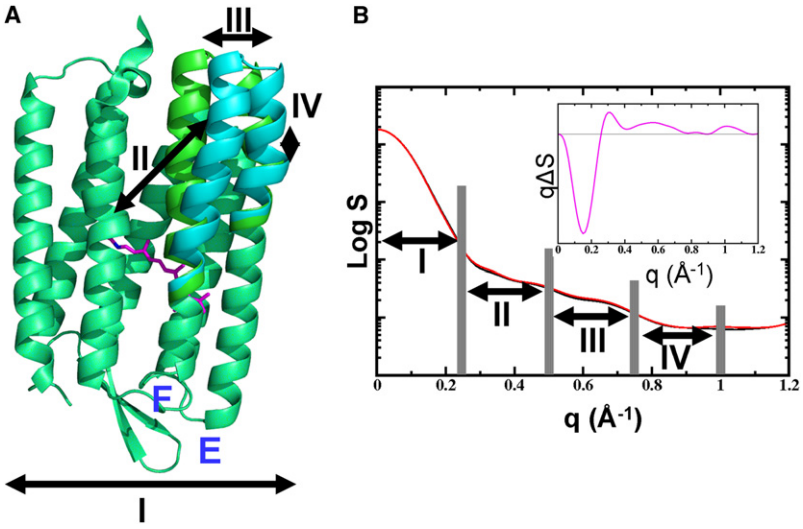

Figure 1. Structural Information Accessible through Time-Resolved Wide-Angle X-Ray Scattering

(A) X-ray structures of bacteriorhodopsin in its resting conformation (green) and for a hypothetical model in which helices E and F are displaced (cyan).

(B) Predicted WAXS spectra from the two structures shown in (A), where $q = 4\pi \sin(\theta)/\lambda = 4\pi/2d$, where 1/d is the resolution quoted in X-ray crystallography. $q = 0.2$ Å^{-1} corresponds approximately to 30 Å resolution and $q = 1.0$ Å^{-1} corresponds approximately to 6 Å resolution. Below $q < 0.2$ Å^{-1} the scattering characterizes the overall dimensions of the protein plus detergent micelle system. For 0.2 Å^{-1} $< q <$ 1.0 Å^{-1} a difference WAXS signal emerges (inset), which reflect α helix movements. A reciprocal relationship between difference features in regions I to IV of q space (B) correlate approximately to distances I to IV in real space (A).

bacteriorhodopsin using time-resolved X-ray diffraction (Koch et al., 1991; Oka et al., 1999, 2000, 2002, 2005; Sass et al., 1997) and neutron (Dencher et al., 1989) and electron (Subramaniam et al., 1993, 1997, 1999; Vonck, 2000) diffraction studies at low temperature could potentially settle this issue (Hirai and Subramaniam, 2009). However, while these techniques have reproducibly indicated difference density peaks associated with helices F (Oka et al., 1999, 2000, 2002, 2005; Sass et al., 1997; Subramaniam et al., 1993, 1997, 1999; Vonck, 2000) and G (Dencher et al., 1989; Koch et al., 1991; Oka et al., 1999, 2000, 2002, 2005; Sass et al., 1997; Subramaniam et al., 1993, 1997, 1999; Vonck, 2000), there are again conflicting conclusions regarding the other global motions with movements associated with helices B (Dencher et al., 1989; Koch et al., 1991; Oka et al., 1999; Sass et al., 1997; Subramaniam et al., 1997), C (Subramaniam et al., 1997), D (Dencher et al., 1989), and E (Dencher et al., 1989; Koch et al., 1991; Vonck, 2000) also suggested. Unlike 3D crystal structures, refined structural coordinates are not provided to indicate the amplitude of the suggested movements and the limited time resolution accessible for the time-resolved 2D X-ray diffraction studies to date (Koch et al., 1991; Oka et al., 1999, 2000, 2002, 2005; Sass et al., 1997) has meant that difference density maps have only been presented for late conformational states.

To characterize in real time the light-driven helical motions of bacteriorhodopsin and to shed light on the dynamical themes that reoccur across other rhodopsin family members, we applied the method of time-resolved wide-angle X-ray scattering (WAXS) to study the structural dynamics of bacteriorhodopsin and proteorhodopsin at room temperature. Time-resolved WAXS has emerged as a powerful technique for visualizing rapid structural rearrangements of small photoactive molecules in solution (Davidsson et al., 2005; Ihee et al., 2005; Neutze et al., 2001; Plech et al., 2004; Vincent et al., 2009), and the method has recently been extended to the study of protein conformational dynamics and protein folding (Cammarata et al., 2008). A hybrid approach has also been suggested to enable both global and local structural changes to be visualized simultaneously (Andersson et al., 2008).

Figure 1 illustrates schematically the structural information that is accessible from proteins using time-resolved WAXS. For $q < 0.2$ Å^{-1} the protein appears globular, with information on the density and approximate size being resolved. Between $0.2 < q < 1.0$ Å^{-1}, helical movements and concerted conformational changes can also be visualized and their time constants determined, whereby the larger the distance between the moving groups the lower the characteristic q values at which the WAXS difference features emerge (Figure 1). For bacteriorhodopsin it also proves possible to exploit the time scale of the observed helical movements so as to address the key question of whether the extracellular H-bond network is disrupted before or after the primary proton transfer event (Figure S2). Moreover, unlike time-resolved diffraction studies of the purple membrane (Koch et al., 1991; Oka et al., 1999, 2000, 2002, 2005; Sass et al., 1997), time-resolved WAXS does not rely on the fortuitous propensity of bacteriorhodopsin to naturally form 2D crystals. Thus, using time-resolved WAXS we are able to also probe the structural dynamics of proteorhodopsin and thereby demonstrate that the global conformational changes of another rhodopsin family member follow similar rearrangements to those occurring in bacteriorhodopsin.

RESULTS

Time-Resolved WAXS Difference Data and Spectral Decomposition

Detergent solubilized, purified, and concentrated samples of both bacteriorhodopsin and proteorhodopsin were mounted within a quartz capillary on the specialized time-resolved beamline ID09B of the European Synchrotron Radiation Facility. The experimental delay, Δt, between the arrival of a green laser pulse and the X-ray pulse were controlled electronically with a temporal domain from 360 ns to 100 ms being sampled. Time-resolved WAXS data were recorded on a CCD camera, integrated in concentric rings, and averaged over multiple repeats. After normalization (Cammarata et al., 2008), data recorded from the sample without laser photoactivation were subtracted to recover the difference signal, $q\Delta S(q,\Delta t)$, as a

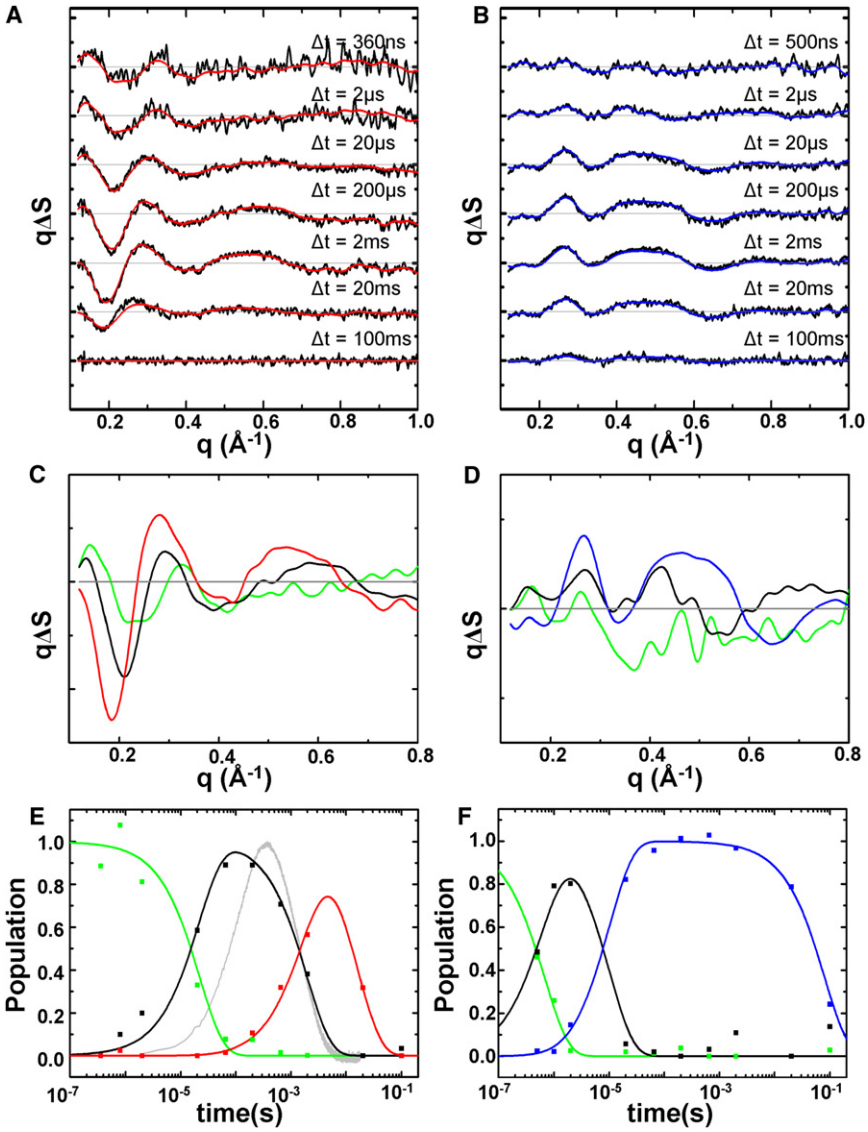

Figure 2. Experimental Time-Resolved Wide-Angle X-Ray Scattering Difference Data

(A and B) Representative difference WAXS data, $q\Delta S(q,\Delta t)$, recorded from samples of bacteriorhodopsin (A) and proteorhodopsin (B) for the indicated time delays following photoexcitation. All curves have had the solvent response to sample heating removed (Figure S3) and the thin gray lines illustrate $\Delta S(q,\Delta t) = 0$.

(C and D) The three basis spectra resulting from the spectral decomposition of the experimental difference data for bacteriorhodopsin (green, early; black, intermediate; red, late basis spectra; all are filtered) and proteorhodopsin (green, early; black, intermediate; blue, late basis spectra).

(E and F) Transient concentrations of these basis spectra for bacteriorhodopsin (E; green, early; black, intermediate; red, late state concentrations) and proteorhodopsin (F; green, early; black, intermediate; blue, late state concentrations). Solid red lines in (A) illustrate that this spectral decomposition accurately describes the experimental data and squares in (E) show the optimal linear combinations of the three basis spectra for all experimental time points. Likewise, the solid blue lines in (B) and squares in (F) make the same comparison for proteorhodopsin. The transient change in absorption at 410 nm, which characterizes the Schiff base deprotonation in bacteriorhodopsin, is shown in (E) as a gray line for comparison. For proteorhodopsin, a high population of deprotonated retinal accumulates only at very high pH (Friedrich et al., 2002).

function of the given time delay. These difference WAXS data, which contain information on structural changes within the protein, also include the solvent response to heating (Georgiou et al., 2006), which was removed as described previously (Cammarata et al., 2008) (Supplemental Experimental Procedures and Figure S3).

Figures 2A and 2B show representative time-resolved difference WAXS data recorded from both proteins. As with time-resolved WAXS studies of small molecules in solution (Davidsson et al., 2005; Ihee et al., 2005; Neutze et al., 2001; Plech et al., 2004) and hemoglobin (Cammarata et al., 2008), oscillations appear in the difference data that correlate directly with protein conformational changes. Although the difference WAXS data are similar for both proteins, there are marked differences in the positions, amplitudes, and time scales of the major features. Spectral decompositions, using three components (early, intermediate, and late), were performed to characterize the time scales and basis spectra associated with the observed evolution of the time-resolved WAXS data (Cammarata et al., 2008) (Supplemental Experimental Procedures), and these three components were sufficient to provide a complete description of the evolution of the data. For bacteriorhodopsin, the early component (Figure 2E, green) decayed rapidly to the intermediate component with a time scale of $\tau_1 = 22$ μs (±2 μs); the intermediate component (Figure 2E, black) decayed to the late component with a rate constant of $\tau_2 = 1.9$ ms (±0.4 ms); whereas the late component (Figure 2E, red) decayed back to the bacteriorhodopsin resting state with a rate constant of $\tau_3 = 16$ ms (±1.5 ms) (Table S1). For proteorhodopsin, three components also provided a complete description of the time-resolved WAXS data but the corresponding time scales were refined to $\tau_1 = 670$ ns (±140 ns), $\tau_2 = 10$ μs (±1 μs), and $\tau_3 = 79$ ms (±4 ms), respectively (Figure 2F). Both proteins returned to their resting state conformation on time scales consistent with spectroscopic characterization (Table S1).

Basis spectra resulting from the optimal spectral decomposition are shown for bacteriorhodopsin and proteorhodopsin in Figures 2C and 2D, respectively. Summing these basis spectra according to their predicted concentrations (Figures 2E and 2F) reproduces the experimental data (Figures 2A [red line] and 2B [blue line]). Conversely, a linear combination of the basis

spectra optimized against all experimental data (Figures 2E and 2F, colored squares) reliably reproduce the concentrations predicted for the transient species (Figures 2E and 2F, colored lines). The extent to which this linear combination reproduces the predicted transient concentrations is a key indicator that the three component spectral decomposition is a valid description of the data.

For the early component of bacteriorhodopsin (Figure 2C, green line) an oscillation below $q < 0.4$ Å^{-1} is apparent. As this evolved the low-resolution oscillations increasing in amplitude, the peak/valley positions shifted slightly, and a new positive difference feature centered at $q = 0.6$ Å^{-1} emerged for the intermediate component (Figure 2C, black line). Finally, for the late component (Figure 2C, red line), the magnitudes of the experimental WAXS differences became even larger and the peak positions again shifted slightly. Because X-ray scattering changes near 0.4 Å$^{-1} < q < 0.6$ Å^{-1} provide a hallmark of helical movements, this data unequivocally demonstrates that significant α helix rearrangements occur in bacteriorhodopsin already on a time scale of microseconds. A similar evolution of the difference WAXS basis spectra is also evident when overlaying the corresponding basis spectra for proteorhodopsin (Figure 2D).

Transient absorption spectroscopy measurements on bacteriorhodopsin at 410 nm (signature of the M intermediate; Figure 2E, gray line) establish that the early-to-intermediate conformational state transition (Figure 2E, green-to-black line) significantly precedes the Schiff base deprotonation. Indeed, the overlap of the intermediate conformational state with the peak populations of the L and early M photocycle intermediates implies that these two spectral intermediates have very similar global conformations, as has previously been argued (Neutze et al., 2002) since they differ chemically only by the movement of a proton from the Schiff base to Asp85. Similarly, the transition from the intermediate-to-late conformational state (Figure 2E, black-to-red line) and reprotonation of the Schiff base occur on similar time scales, such that the late conformational state describes the late M intermediate, the N intermediate, and the decay of the O intermediate. Again we conclude that spectrally distinct intermediates involve rather similar α-helical conformational changes.

In proteorhodopsin, which lacks the L intermediate, the primary proton transfer event occurs approximately an order of magnitude faster than for bacteriorhodopsin (Friedrich et al., 2002) (Figures S1B and S1C). This correlates with our structural observation that the late conformational state arises much faster in proteorhodopsin than in bacteriorhodopsin (Figures 2E and 2F and Table S1). Likewise, the significantly broader plateau for the late conformational state of proteorhodopsin (Figure 2E) is consistent with its slower spectral relaxation back to the resting state.

Structural Refinement of the Intermediate and Late Bacteriorhodopsin Conformations

Time-resolved WAXS studies of the hemoglobin:carbon monoxide complexes have established that experimentally observed X-ray scattering differences directly correlate with protein conformational changes (Cammarata et al., 2008), as several transient structures of photoactivated small molecules in solution have been successfully refined against time-resolved WAXS difference data (Davidsson et al., 2005; Ihee et al., 2005; Plech et al., 2004; Vincent et al., 2009). Unlike the earlier studies of the hemoglobin:carbon monoxide complex, however, none of the WAXS differences predicted from the deposited intermediate state structures of bacteriorhodopsin yield an entirely satisfactory match to either the intermediate or late conformational states (Figure S4). To quantify the agreement between the WAXS differences predicted from the deposited intermediate state structures and experiment, we calculated an R factor developed in analogy with the standard R factor in protein crystallography (Experimental Procedures, Equation 1). These values are tabulated in Table 1 and vary from 54% to 100%, although some structures with relatively low R factors had important α-helical and loop regions missing from the model (residues 154–175 and 223–232 [Luecke et al., 1999a] and residues 64–77 (Rouhani et al., 2001]).

To objectively model the experimental WAXS difference data we developed an iterative optimization procedure that combined isomerized retinal with movements of helix A, both halves of helix B, both the extracellular (Edman et al., 2004) and the cytoplasmic half of helix C, all of helix D, and the cytoplasmic portions of helices E, F, and G (Subramaniam and Henderson, 2000) (Figure S4). Candidate models were then scored according to an R factor calculated against both basis spectra recovered for the intermediate and late conformational states (Supplemental Experimental Procedures, Equation 8). The early conformational state basis spectra were excluded from this refinement procedure due to their poor signal-to-noise ratio (Table S4) and the possibility that transient thermal equilibration also influenced the sub-microsecond data (Georgiou et al., 2006) ($t_{1/2}$ ~200 ns for thermal equilibration for both experiments). While avoiding excessive degrees of freedom (Supplemental Experimental Procedures) this refinement protocol comes with the caveat that the extracellular and cytoplasmic movements are modeled as linear rigid body motions of helical regions, whereas, in reality, more complex breathing motions of the protein may be involved.

From this set of candidate helical movements, a hierarchy assigning the significance of each motion was developed according to the drop in R factor achieved as the motion was introduced into the structural refinement procedure. When only one helical movement at a time was considered (Table S3), an outwards tilt of the cytoplasmic halves of helices E and F produced the most significant decrease in R factor to 55%. Covarying this movement with an inward flex of the extracellular half of helix C further decreased the R factor to 32%. Although a third iteration of this approach resulted in a further modest drop in the R factor, a comparable decrease could also be achieved (to 29%) by repeating the previous search using a finer grid. We therefore conclude that an outward tilt of the cytoplasmic halves of helices E and F plus an inwards flex of the cytoplasmic portion of helix C are necessary and sufficient to describe the photocycle of bacteriorhodopsin when probed by time-resolved WAXS.

As summarized in Table 1 and Table S4, an optimal fit to the experimental data (Figure 3A) was recovered when the early bacteriorhodopsin conformational state exhibited a 1.0 Å ± 0.3 Å flex for the extracellular half of helix C toward the retinal (Edman et al., 2004; Royant et al., 2000) and an outwards tilt of 2.2 Å ± 0.4 Å for the cytoplasmic half of helix F (Subramaniam and Henderson, 2000). These movements became significantly larger during the transition to the latter conformational state, for which

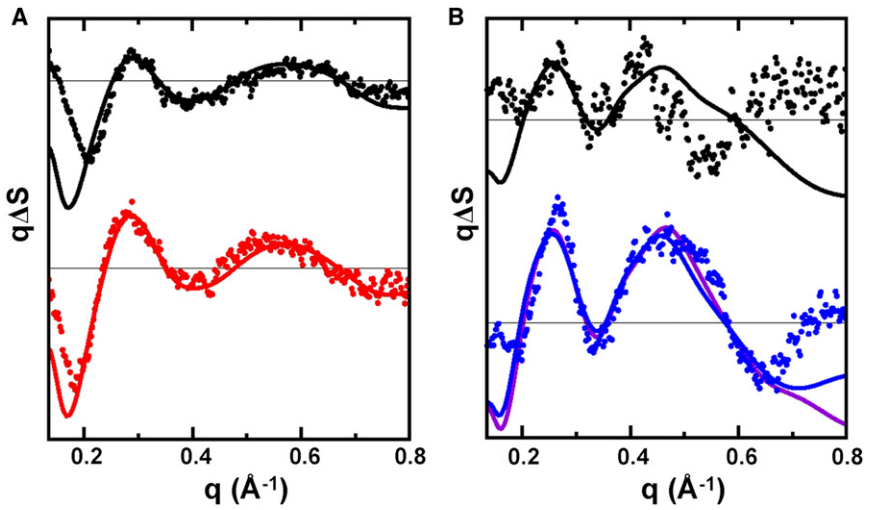

Figure 3. Structural Analysis of the Transient WAXS Difference Data

(A) Best fit difference WAXS changes predicted (thick lines) for bacteriorhodopsin superimposed on the intermediate (black) and late (red) components of the experimental difference data (circles). An R factor of 34% and 25% was obtained for these two fits, respectively (Table 1).

(B) Best fit difference WAXS changes predicted (thick lines) for proteorhodopsin superimposed on the intermediate (black) and late (blue) components of the experimental difference data (circles). An R factor of 81% and 33% was recovered for these two curves, respectively (Table 1). Refinement against the late conformational state of proteorhodopsin alone gave an R factor of 28% (purple line).

the cytoplasmic half of helix F became displaced by 2.9 Å ± 0.5 Å and the extracellular half of helix C flexed inwards by 1.5 ± 0.2 Å. Not only were the individual R factor values for each of these refined conformational states (34% for the intermediate and 25% for late conformational states) significantly better than those predicted from any deposited intermediate state structure (Table 1) but there is also clear agreement between the predicted and experimental curves (Figure 3A).

Structural Refinement of the Late Proteorhodopsin Conformation

Because no X-ray structure is available for proteorhodopsin, structural analysis began from a homology model (Rangarajan et al., 2007). An identical refinement protocol as described for bacteriorhodopsin was then applied to the time-resolved difference WAXS data recorded from proteorhodopsin using the same displacement vectors. Iterative refinement cycles again revealed that an outwards movement of the cytoplasmic halves of helices E and F produced the most significant decrease in R factor to 83% when only one motion was allowed (Table S3). As with bacteriorhodopsin, a second iteration also assigned the inwards flex of the extracellular half of helix C as the next most significant movement (R factor decreased to 66%), with the capping motion of the cytoplasmic portion of helix G emerging as a final significant component of the motion (R factor decreased to 51%). When the intermediate and late conformational states are considered separately, however, it is apparent that the R factor for the intermediate conformational state of proteorhodopsin (81%) was significantly worse than that recovered for its late conformation (33%), which is also reflected in the poorer fit (Figure 3B) and signal-to-noise of this data (Table S2). To avoid the results of structural refinement for proteorhodopsin being influenced by the failure of the intermediate state model, we repeated the refinement procedure against the late conformational state alone, recovering a final R factor of 28% (Table 1 and Figure 3B, purple line).

From this procedure we conclude (Table S4) that an outward tilt of the cytoplasmic half of helices E (0.8 Å ± 0.3 Å) and F (2.6 Å ± 0.6 Å), an inwards flex of the extracellular portion of helix C (0.9 Å ± 0.4 Å), as well as a capping motion of the cytoplasmic portion of helix G (1.2 Å ± 0.3 Å), can be observed with confidence from the WAXS difference data for late conformational state of proteorhodopsin, whereas the specific conformation of the proteorhodopsin intermediate conformational state could not be refined to an acceptable R factor. It is also striking that the major components of the observed helical movements are the same for bacteriorhodopsin and proteorhodopsin, as are the predicted magnitudes of the movements of helix F also in agreement within errors, despite the very obvious differences in the difference WAXS basis spectra for their respective late conformational states.

Uniqueness of the Structural Solution

Figure S6 illustrates the difference WAXS curves predicted for bacteriorhodopsin when following this iterative refinement protocol, providing an intuitive representation of why this structural refinement procedure converged upon the movements of helices E, F, and C. Although it is clear from this representation why these motions were selected, and the final R factor values for the intermediate (34%) and late (25%) conformational states of bacteriorhodopsin are significantly better than all those recovered from any deposited crystallographic structure (Table 1), it may be questioned whether this analysis locates a global minimum or if any random combination of helical movements would ultimately converge to an acceptable R value.

To test this possibility we applied CONCOORD (de Groot et al., 1997) to generate 1000 random candidate structural models for conformational changes in bacteriorhodopsin and calculated the R factors recovered from this random set of structures against the intermediate and late conformational state basis spectra. These values are plotted in Figures 4A and 4B (black squares) as a function of the root mean square deviation of C_α atoms from the starting structure and show a distribution of R factors from 55% to 95%. When repeating this analysis, but instead starting from the refined structural models for these two conformational states, we find that the distribution of R factors are on average approximately 25% lower (Figures 4A and 4B, red squares, ranging from 35% to 70%) and the further one departs from the refined structures the worse the R factor becomes. An identical analysis of structures randomly generated about the

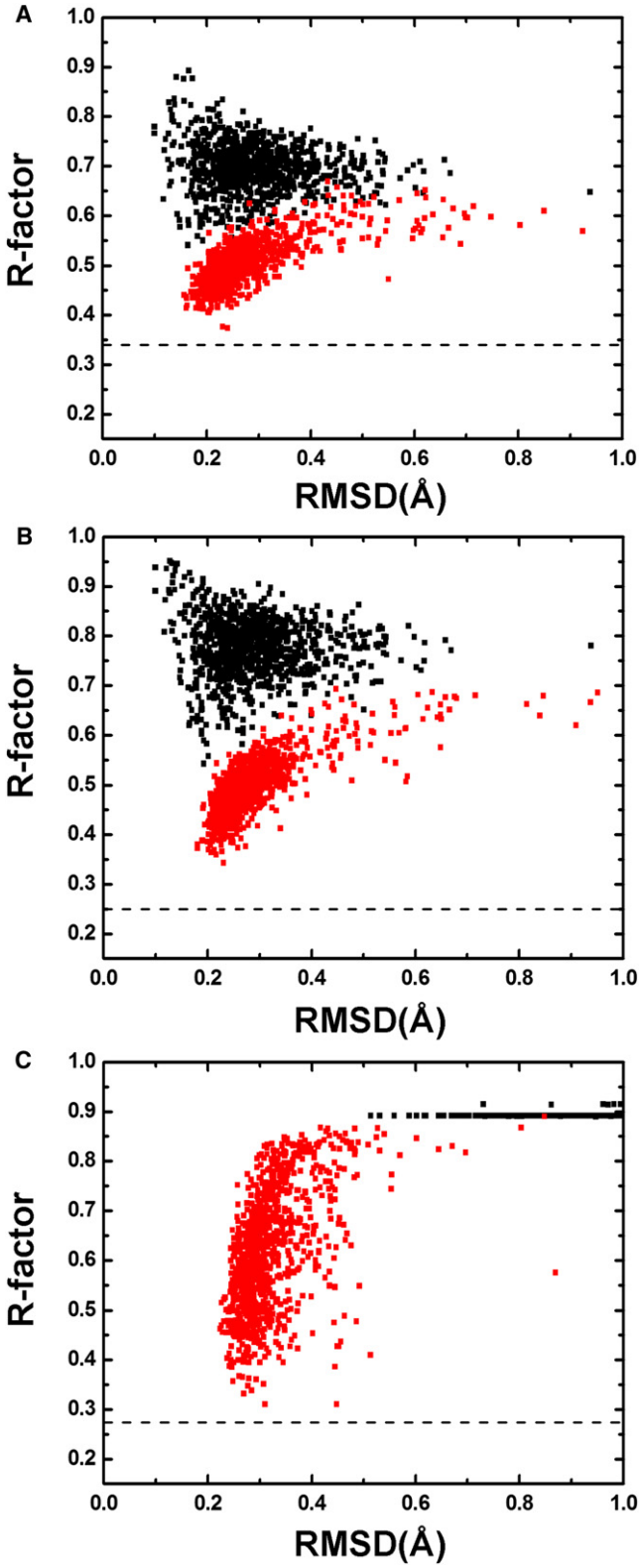

Figure 4. Analysis of R Factor Distributions from Randomly Generated Structures

(A) R factor values determined against the bacteriorhodopsin intermediate conformational state basis spectrum when 1000 random structures are generated starting from the bacteriorhodopsin resting state structure (black) and starting from the refined intermediate state structure (red). Rmsd values represent the average root mean square deviation of C_α atoms for each random structure relative to the starting model.

(B) A similar R factor distribution for 1000 random structures as shown in (A), but calculated against the bacteriorhodopsin late conformational state basis spectrum and starting from the bacteriorhodopsin resting state (black) and refined late conformational state model (red).

(C) A similar R factor distribution as shown in (A) and (B), but calculated against the proteorhodopsin late conformational state basis spectrum and starting from the resting (black) and late (red) conformational states of proteorhodopsin when generating random structures.

Dashed lines indicate the final R-factor achieved during structural refinement.

proteorhodopsin resting conformation and its refined late conformational state yielded a similar conclusion (Figure 4C). In that case, however, no random structures generated from the resting state conformation gave an R factor lower than 89%. Thus we conclude that the refinement procedure developed here reliably converges toward a global minimum.

Application of Time-Resolved WAXS to Other Systems

From these results on bacteriorhodopsin and proteorhodopsin, as well as previous work on hemoglobin:carbon monoxide complexes (Cammarata et al., 2008), it is of value to consider the extent to which time-resolved WAXS may be applied to other membrane protein systems such as transporters, pumps, and gated channels for which conformational changes are believed to occur. Because most systems are not naturally photoactive, other triggering protocols will need to be developed such as microfluidics stopped flow devices or the use of caged compounds (Giovannardi et al., 1998). Although it should be straightforward to extract basis spectra and refine the rate constants associated with transient conformational changes, a more significant challenge will be the structural interpretation of WAXS difference data when there is little knowledge regarding specific conformational changes. Computational tools such as course grain models (Stumpff-Kane et al., 2008; Tozzini, 2005), molecular dynamics simulations and normal mode analysis (Stumpff-Kane et al., 2008), and the geometric sampling of protein conformational transitions (Seeliger et al., 2007) could all be implemented in connection with structural refinement and converge upon transient protein conformations with a minimum number of additional chemical assumptions.

DISCUSSION

Figure 5 overviews the mechanistic picture to emerge from these time-resolved WAXS studies of bacteriorhodopsin at room temperature. As is apparent from Table 1, the light-induced conformational changes are appreciably larger at room temperature when the protein is not constrained by a 3D crystal lattice. More significantly, however, is that the primary proton transfer event from the Schiff base to Asp85 does not mark a boundary separating two distinctly different types of motion. Rather, the inward collapse of the extracellular half of the proton transport channel (Royant et al., 2000) and the opening of the cytoplasmic half (Subramaniam and Henderson, 2000) arise as two aspects of the same basic motion, with the primary proton transfer event marking a threshold after which the magnitudes of these

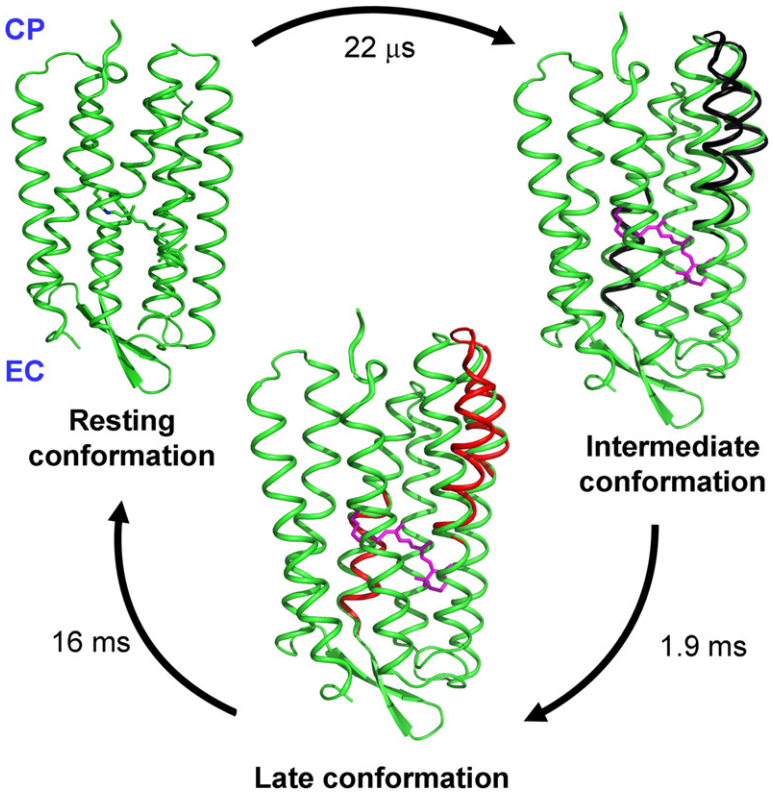

Figure 5. Significant Conformational Changes Observed During the Photocycle of Bacteriorhodopsin
The resting conformation (green), an intermediate conformational state (black), and a late conformational state (red) are represented. For comparison, the resting conformation is superimposed on the intermediate and late conformational states. Significant outwards movement of the cytoplasmic portions of helices E and F and an inwards movement of helix C toward the Schiff base occur already within 22 μs of photoactivation. These motions increase in amplitude by approximately 50% following the deprotonation of the Schiff base. A similar picture describing the conformational dynamics of proteorhodopsin also emerges. Two movies illustrating the bacteriorhodopsin movements are available in the Supplemental Data (Movies S1 and S2).

motions grow approximately 50%. From the different time scales associated with the intermediate and late conformational states of bacteriorhodopsin (Figure 2E) we conclude that a significant energy barrier exists that can only be traversed following Schiff base deprotonation. This picture both simplifies the description of the protein conformational dynamics and supports intuition, since all protein motions derive from a steric clash with photoisomerized retinal. As the Schiff base deprotonates the retinal straightens (Subramaniam and Henderson, 2000) and an electrostatic attraction between the positively charged Schiff base to the negatively charged Asp85 is lost. Both effects allow the retinal to be displaced further toward the cytoplasm and consequently drive larger protein movements.

In the resting state of bacteriorhodopsin, the extracellular half of the protein is held rigid by a complex network of water-mediated H-bond interactions (Belrhali et al., 1999) primarily connecting helices C and G (Figure S2). As found in intermediate trapping studies (Edman et al., 2004; Royant et al., 2000), a conformational flex of the extracellular half of helix C toward the proton pumping channel cannot occur unless this extended H-bond network is disrupted (Figure S2). Using time-resolved WAXS we observe that a significant inwards flex of helix C toward the proton pumping channel occurs prior to the Schiff base deprotonation event. Accordingly, a major rearrangement of water molecules must already have happened on this time scale, which both allows helix C to flex and changes the local chemical environment of the Schiff base and Asp85, such that the pKa of the Schiff base drops and that of Asp85 increases. These dynamical changes in H-bond interactions thus set the stage for spontaneous proton transfer between these two groups and should be regarded a major cause of this critical event in the bacteriorhodopsin photocycle (Bondar et al., 2006; Neutze et al., 2002).

Comparison of the major structural findings for bacteriorhodopsin and proteorhodopsin (Table 1 and Table S4) shows that the rearrangements of secondary structural elements that occur during proton pumping by archaeal bacteriorhodopsin also arise in marine bacterial proteorhodopsin. Given the vast biomass of bacterioplankton in the world's oceans, we conclude that this basic structural mechanism drives a significant input of energy into the marine biosphere (Beja et al., 2000, 2001; Gomez-Consarnau et al., 2007). Moreover, our observation that these conformational changes are conserved across phylogenetically separated organisms implies underlying dynamical principles that are almost certainly exploited in other biological functions such as signal transduction (Royant et al., 2001), ion transport (Kolbe et al., 2000), and ion gating (Nagel et al., 2002). In this context it is striking that the G protein-coupled receptor visual rhodopsin, which is only distantly related to the bacterial rhodopsins, is also activated by a similar outwards movement of helices E and F (Scheerer et al., 2008), illustrating how common conformational rearrangements can be exploited in distinct cellular contexts.

EXPERIMENTAL PROCEDURES

Data Collection

Concentrated samples of detergent-solubilized and -purified bacteriorhodopsin and proteorhodopsin were transferred into a quartz capillary and mounted on the dedicated time-resolved X-ray diffraction beamline ID09B of the European Synchrotron Radiation Facility using a setup essentially identical to that described previously (Cammarata et al., 2008) (for details see Supplemental Experimental Procedures).

Data Reduction

Data from two experimental runs were integrated using FIT2D (Hammersley, 1997) and normalized according to the total scattering recorded at q = 1.5-1.7 $Å^{-1}$. After normalization, $\Delta S(q,\Delta t)$ for each time delay (Δt) was calculated by subtracting data taken for a negative time delay (i.e., the laser pulse arrives 50 μs after the X-ray pulse; for details see Supplemental Experimental Procedures). Typically 30 to 130 images were recorded and merged for each Δt and difference data $\Delta S(q,\Delta t)$, which deviated by more than 3.5 σ from the average

ΔS(q,Δt), were rejected (typically 15% of the data). For each of the averaged data sets the solvent response to sample heating was then removed (Figure S3) and representative data are shown in Figures 1A and 1B. Basis spectra for the early and late states (Figure 2) were extracted by spectral decomposition assuming a simple sequential photocycle model with three transients called the early, intermediate, and late conformational states (for details see Supplemental Experimental Procedures).

Structural Modeling

An R factor was defined as follows to analyze the agreement between the difference WAXS curves predicted from structural models and the experimental difference WAXS data:

$$R-\text{factor} = \sum \sqrt{\left(\Delta S^{\text{theory}} - \Delta S^{\text{expt}}\right)^2} \Big/ \sum \sqrt{\left(\Delta S^{\text{expt}}\right)^2} \quad (1)$$

where ΔS^{expt} represents a specific difference WAXS basis spectra recovered from spectral decomposition of the experimental data and ΔS^{theory} represents the difference WAXS curve predicted from a given structural model. An overall scaling factor plus a small constant offset (which allows for uncertainty in the temperature correction) were included as free variables to optimize when recovering the R factor values given in Table 1.

For structural refinement, this R factor was modified slightly to allow the simultaneous optimization of two structural models against the basis spectra (ΔS^{expt}) recovered for the intermediate and late conformational states (Supplemental Experimental Procedures, Equation 8). The deposited 1.9 Å structure of bacteriorhodopsin (Belrhali et al., 1999) and a slightly modified homology model of proteorhodopsin (Rangarajan et al., 2007) (shifted in sequence by one Cα atom position in helix F toward the cytoplasm so as to place Trp197 above the C20 retinal methyl group) were used as starting points for structural analysis. Structural refinement of a candidate set of helical movements was then performed against the intermediate and late state basis spectra (Figure 3) as described in the text (see also Supplemental Experimental Procedures) using CRYSOL to predict the X-ray scattering curves (Svergun et al., 1995). In this analysis, the membrane protein models were placed within a hydrophobic membrane bilayer and a B factor term was introduced to account for the high level of disorder of this bilayer (see Supplemental Experimental Procedures for more details). Uncertainties in the magnitudes of the refined helical movements (Table S3) were estimated from the standard deviations of the 50 best solutions (of 46,656 possible combinations).

Nonlinearity in the predicted X-ray scattering curves with the amplitude of the helical movements (Figure S7) enabled this structural refinement to proceed without the need to first specify the photoexcited populations (determined afterwards as 35% ± 10% for bacteriorhodopisin and 20% ± 7% for proteorhodopsin; see Supplemental Experimental Procedures). The difference X-ray scattering data at low resolution could be better modeled by incorporating a dynamic response of the surrounding membrane (micelle), such as a slight change in density in response to protein conformational changes (Figure S8). These low resolution considerations, however, had no influence on the results of structural refinement.

SUPPLEMENTAL DATA

Supplemental data include Supplemental Experimental Procedures, eight figures, five tables, and two movies and can be found with this article online at http://www.cell.com/structure/supplemental/S0969-2126(09)00290-1.

ACKNOWLEDGMENTS

We thank Robert Birge for providing coordinates for a model of proteorhodopsin developed from homology with bacteriorhodopsin. We are indebted to Philip Anfinrud and Friedrich Schotte for the design of the field-programmable gate array-based timing system used in these experiments. We acknowledge financial support from the Swedish Science Research Council (VR), the Swedish Strategic Research Foundation, the Human Frontier Science Program, the European Commission Marie Currie Postdoctoral Fellowship Programme, and the Chalmers Bioscience Programme. The authors declare no competing financial interests.

Received: May 19, 2009
Revised: July 7, 2009
Accepted: July 9, 2009
Published: September 8, 2009

REFERENCES

Andersson, M., Vincent, J., van der Spoel, D., Davidsson, J., and Neutze, R. (2008). A proposed time-resolved X-ray scattering approach to track local and global conformational changes in membrane transport proteins. Structure *16*, 21–28.

Beja, O., Aravind, L., Koonin, E.V., Suzuki, M.T., Hadd, A., Nguyen, L.P., Jovanovich, S.B., Gates, C.M., Feldman, R.A., Spudich, J.L., et al. (2000). Bacterial rhodopsin: evidence for a new type of phototrophy in the sea. Science *289*, 1902–1906.

Beja, O., Spudich, E.N., Spudich, J.L., Leclerc, M., and DeLong, E.F. (2001). Proteorhodopsin phototrophy in the ocean. Nature *411*, 786–789.

Belrhali, H., Nollert, P., Royant, A., Menzel, C., Rosenbusch, J.P., Landau, E.M., and Pebay-Peyroula, E. (1999). Protein, lipid and water organization in bacteriorhodopsin crystals: a molecular view of the purple membrane at 1.9 A resolution. Structure *7*, 909–917.

Bondar, A.-N., Smith, J.C., and Fischer, S. (2006). Structural and energetic determinants of primary proton transfer in bacteriorhodopsin. Photochem. Photobiol. Sci. *5*, 547–552.

Cammarata, M., Levantino, M., Schotte, F., Anfinrud, P.A., Ewald, F., Choi, J., Cupane, A., Wulff, M., and Ihee, H. (2008). Tracking the structural dynamics of proteins in solution using time-resolved wide-angle X-ray scattering. Nat. Methods *5*, 881–886.

Davidsson, J., Poulsen, J., Cammarata, M., Georgiou, P., Wouts, R., Katona, G., Jacobson, F., Plech, A., Wulff, M., Nyman, G., and Neutze, R. (2005). Structural determination of a transient isomer of CH_2I_2 by picosecond X-ray diffraction. Phys. Rev. Lett. *94*, 245503.

de Groot, B.L., van Aalten, D.M., Scheek, R.M., Amadei, A., Vriend, G., and Berendsen, H.J. (1997). Prediction of protein conformational freedom from distance constraints. Proteins *29*, 240–251.

Dencher, N.A., Dresselhaus, D., Zaccai, G., and Buldt, G. (1989). Structural changes in bacteriorhodopsin during proton translocation revealed by neutron diffraction. Proc. Natl. Acad. Sci. USA *86*, 7876–7879.

Edman, K., Nollert, P., Royant, A., Belrhali, H., Pebay-Peyroula, E., Hajdu, J., Neutze, R., and Landau, E.M. (1999). High-resolution X-ray structure of an early intermediate in the bacteriorhodopsin photocycle. Nature *401*, 822–826.

Edman, K., Royant, A., Larsson, G., Jacobson, F., Taylor, T., van der Spoel, D., Landau, E.M., Pebay-Peyroula, E., and Neutze, R. (2004). Deformation of helix C in the low temperature L-intermediate of bacteriorhodopsin. J. Biol. Chem. *279*, 2147–2158.

Facciotti, M.T., Rouhani, S., Burkard, F.T., Betancourt, F.M., Downing, K.H., Rose, R.B., McDermott, G., and Glaeser, R.M. (2001). Structure of an early intermediate in the M-state phase of the bacteriorhodopsin photocycle. Biophys. J. *81*, 3442–3455.

Friedrich, T., Geibel, S., Kalmbach, R., Chizhov, I., Ataka, K., Heberle, J., Engelhard, M., and Bamberg, E. (2002). Proteorhodopsin is a light-driven proton pump with variable vectoriality. J. Mol. Biol. *321*, 821–838.

Georgiou, P., Vincent, J., Andersson, M., Wöhri, A.B., Gourdon, P., Poulsen, J., Davidsson, J., and Neutze, R. (2006). Picosecond calorimetry: time-resolved x-ray diffraction studies of liquid CH_2Cl_2. J. Phys. Chem. *124*, 234507.

Giovannardi, S., Lando, L., and Peres, A. (1998). Flash photolysis of caged compounds: casting light on physiological processes. News Physiol. Sci. *13*, 251–255.

Gomez-Consarnau, L., Gonzalez, J.M., Coll-Llado, M., Gourdon, P., Pascher, T., Neutze, R., Pedros-Alio, C., and Pinhassi, J. (2007). Light stimulates growth of proteorhodopsin-containing marine Flavobacteria. Nature *445*, 210–213.

Hammersley, A.P. (1997). FIT2D: An Introduction and Overview. ESRF Internal Report, http://www.esrf.eu/computing/scientific/FIT2D/FIT2D_INTRO/fit2d.html.

Haupts, U., Tittor, J., and Oesterhelt, D. (1999). Closing in on bacteriorhodopsin: progress in understanding the molecule. Annu. Rev. Biophys. Biomol. Struct. *28*, 367–399.

Henderson, R., and Unwin, P.N. (1975). Three-dimensional model of purple membrane obtained by electron microscopy. Nature *257*, 28–32.

Henderson, R., Baldwin, J.M., Ceska, T.A., Zemlin, F., Beckmann, E., and Downing, K.H. (1990). Model for the structure of bacteriorhodopsin based on high-resolution electron cryo-microscopy. J. Mol. Biol. *213*, 899–929.

Hirai, T., and Subramaniam, S. (2009). Protein conformational changes in the bacteriorhodopsin photocycle: comparison of findings from electron and X-ray crystallographic analyses. PLoS ONE *4*, e5769.

Ihee, H., Lorenc, M., Kim, T.K., Kong, Q.Y., Cammarata, M., Lee, J.H., Bratos, S., and Wulff, M. (2005). Ultrafast x-ray diffraction of transient molecular structures in solution. Science *309*, 1223–1227.

Koch, M.H., Dencher, N.A., Oesterhelt, D., Plohn, H.J., Rapp, G., and Buldt, G. (1991). Time-resolved X-ray diffraction study of structural changes associated with the photocycle of bacteriorhodopsin. EMBO J. *10*, 521–526.

Kolbe, M., Besir, H., Essen, L.O., and Oesterhelt, D. (2000). Structure of the light-driven chloride pump halorhodopsin at 1.8 A resolution. Science *288*, 1390–1396.

Kouyama, T., Nishikawa, T., Tokuhisa, T., and Okumura, H. (2004). Crystal structure of the L intermediate of bacteriorhodopsin: evidence for vertical translocation of a water molecule during the proton pumping cycle. J. Mol. Biol. *335*, 531–546.

Kuhlbrandt, W. (2000). Bacteriorhodopsin—the movie. Nature *406*, 569–570.

Landau, E.M., and Rosenbusch, J.P. (1996). Lipidic cubic phases: a novel concept for the crystallization of membrane proteins. Proc. Natl. Acad. Sci. USA *93*, 14532–14535.

Lanyi, J., and Schobert, B. (2002). Crystallographic structure of the retinal and the protein after deprotonation of the Schiff base: the switch in the bacteriorhodopsin photocycle. J. Mol. Biol. *321*, 727–737.

Lanyi, J.K., and Schobert, B. (2003). Mechanism of proton transport in bacteriorhodopsin from crystallographic structures of the K, L, M_1, M_2, and M_2' intermediates of the photocycle. J. Mol. Biol. *328*, 439–450.

Lanyi, J.K., and Schobert, B. (2006). Propagating structural perturbation inside bacteriorhodopsin: crystal structures of the M state and the D96A and T46V mutants. Biochemistry *45*, 12003–12010.

Lanyi, J.K., and Schobert, B. (2007). Structural changes in the L photointermediate of bacteriorhodopsin. J. Mol. Biol. *365*, 1379–1392.

Luecke, H., Schobert, B., Richter, H.T., Cartailler, J.P., and Lanyi, J.K. (1999a). Structural changes in bacteriorhodopsin during ion transport at 2 angstrom resolution. Science *286*, 255–261.

Luecke, H., Schobert, B., Richter, H.T., Cartailler, J.P., and Lanyi, J.K. (1999b). Structure of bacteriorhodopsin at 1.55 A resolution. J. Mol. Biol. *291*, 899–911.

Luecke, H., Schobert, B., Cartailler, J.P., Richter, H.T., Rosengarth, A., Needleman, R., and Lanyi, J.K. (2000). Coupling photoisomerization of retinal to directional transport in bacteriorhodopsin. J. Mol. Biol. *300*, 1237–1255.

Matsui, Y., Sakai, K., Murakami, M., Shiro, Y., Adachi, S., Okumura, H., and Kouyama, T. (2002). Specific damage induced by X-ray radiation and structural changes in the primary photoreaction of bacteriorhodopsin. J. Mol. Biol. *324*, 469–481.

Nagel, G., Ollig, D., Fuhrmann, M., Kateriya, S., Musti, A.M., Bamberg, E., and Hegemann, P. (2002). Channelrhodopsin-1: a light-gated proton channel in green algae. Science *296*, 2395–2398.

Neutze, R., Wouts, R., Techert, S., Davidsson, J., Kocsis, M., Kirrander, A., Schotte, F., and Wulff, M. (2001). Visualizing photochemical dynamics in solution through picosecond x-ray scattering. Phys. Rev. Lett. *87*, 195508.

Neutze, R., Pebay-Peyroula, E., Edman, K., Royant, A., Navarro, J., and Landau, E.M. (2002). Bacteriorhodopsin: a high-resolution structural view of vectorial proton transport. Biochim. Biophys. Acta *1565*, 144–167.

Oesterhelt, D., and Stoeckenius, W. (1971). Rhodopsin-like protein from the purple membrane of *Halobacterium halobium*. Nat. New Biol. *233*, 149–152.

Oka, T., Kamikubo, H., Tokunaga, F., Lanyi, J.K., Needleman, R., and Kataoka, M. (1999). Conformational change of helix G in the bacteriorhodopsin photocycle: investigation with heavy atom labeling and x-ray diffraction. Biophys. J. *76*, 1018–1023.

Oka, T., Yagi, N., Fujisawa, T., Kamikubo, H., Tokunaga, F., and Kataoka, M. (2000). Time-resolved x-ray diffraction reveals multiple conformations in the M-N transition of the bacteriorhodopsin photocycle. Proc. Natl. Acad. Sci. USA *97*, 14278–14282.

Oka, T., Yagi, N., Tokunaga, F., and Kataoka, M. (2002). Time-resolved X-ray diffraction reveals movement of F helix of D96N bacteriorhodopsin during M-MN transition at neutral pH. Biophys. J. *82*, 2610–2616.

Oka, T., Inoue, K., Kataoka, M., and Yagi, N. (2005). Structural transition of bacteriorhodopsin is preceded by deprotonation of Schiff base: microsecond time-resolved x-ray diffraction study of purple membrane. Biophys. J. *88*, 436–442.

Palczewski, K., Kumasaka, T., Hori, T., Behnke, C.A., Motoshima, H., Fox, B.A., Le Trong, I., Teller, D.C., Okada, T., Stenkamp, R.E., et al. (2000). Crystal structure of rhodopsin: A G protein-coupled receptor. Science *289*, 739–745.

Plech, A., Wulff, M., Bratos, S., Mirloup, F., Vuilleumier, R., Schotte, F., and Anfinrud, P.A. (2004). Visualizing chemical reactions in solution by picosecond x-ray diffraction. Phys. Rev. Lett. *92*, 125505.

Rangarajan, R., Galan, J.F., Whited, G., and Birge, R.R. (2007). Mechanism of spectral tuning in green-absorbing proteorhodopsin. Biochemistry *46*, 12679–12686.

Rouhani, S., Cartailler, J.P., Facciotti, M.T., Walian, P., Needleman, R., Lanyi, J.K., Glaeser, R.M., and Luecke, H. (2001). Crystal structure of the D85S mutant of bacteriorhodopsin: model of an O-like photocycle intermediate. J. Mol. Biol. *313*, 615–628.

Royant, A., Edman, K., Ursby, T., Pebay-Peyroula, E., Landau, E.M., and Neutze, R. (2000). Helix deformation is coupled to vectorial proton transport in the photocycle of bacteriorhodopsin. Nature *406*, 645–648.

Royant, A., Nollert, P., Edman, K., Neutze, R., Landau, E.M., Pebay-Peyroula, E., and Navarro, J. (2001). X-ray structure of sensory rhodopsin II at 2.1-A resolution. Proc. Natl. Acad. Sci. USA *98*, 10131–10136.

Sass, H.J., Schachowa, I.W., Rapp, G., Koch, M.H., Oesterhelt, D., Dencher, N.A., and Buldt, G. (1997). The tertiary structural changes in bacteriorhodopsin occur between M states: X-ray diffraction and Fourier transform infrared spectroscopy. EMBO J. *16*, 1484–1491.

Sass, H.J., Buldt, G., Gessenich, R., Hehn, D., Neff, D., Schlesinger, R., Berendzen, J., and Ormos, P. (2000). Structural alterations for proton translocation in the M state of wild-type bacteriorhodopsin. Nature *406*, 649–653.

Scheerer, P., Park, J.H., Hildebrand, P.W., Kim, Y.J., Krauss, N., Choe, H.W., Hofmann, K.P., and Ernst, O.P. (2008). Crystal structure of opsin in its G-protein-interacting conformation. Nature *455*, 497–502.

Schobert, B., Cupp-Vickery, J., Hornak, V., Smith, S., and Lanyi, J. (2002). Crystallographic structure of the K intermediate of bacteriorhodopsin: conservation of free energy after photoisomerization of the retinal. J. Mol. Biol. *321*, 715–726.

Schobert, B., Brown, L.S., and Lanyi, J.K. (2003). Crystallographic structures of the M and N intermediates of bacteriorhodopsin: assembly of a hydrogen-bonded chain of water molecules between Asp-96 and the retinal Schiff base. J. Mol. Biol. *330*, 553–570.

Seeliger, D., Haas, J., and de Groot, B.L. (2007). Geometry-based sampling of conformational transitions in proteins. Structure *15*, 1482–1492.

Stumpff-Kane, A.W., Maksimiak, K., Lee, M.S., and Feig, M. (2008). Sampling of near-native protein conformations during protein structure refinement using a coarse-grained model, normal modes, and molecular dynamics simulations. Proteins *70*, 1345–1356.

Subramaniam, S., and Henderson, R. (2000). Molecular mechanism of vectorial proton translocation by bacteriorhodopsin. Nature *406*, 653–657.

Subramaniam, S., Gerstein, M., Oesterhelt, D., and Henderson, R. (1993). Electron diffraction analysis of structural changes in the photocycle of bacteriorhodopsin. EMBO J. *12*, 1–8.

Subramaniam, S., Faruqi, A.R., Oesterhelt, D., and Henderson, R. (1997). Electron diffraction studies of light-induced conformational changes in the

Leu-93 –> Ala bacteriorhodopsin mutant. Proc. Natl. Acad. Sci. USA *94*, 1767–1772.

Subramaniam, S., Lindahl, M., Bullough, P., Faruqi, A.R., Tittor, J., Oesterhelt, D., Brown, L., Lanyi, J., and Henderson, R. (1999). Protein conformational changes in the bacteriorhodopsin photocycle. J. Mol. Biol. *287*, 145–161.

Svergun, D., Barberato, C., and Koch, M.H.J. (1995). CRYSOL - a Program to Evaluate X-ray Solution Scattering of Biological Macromolecules from Atomic Coordinates. J. Appl. Crystallogr. *28*, 768–773.

Takeda, K., Matsui, Y., Kamiya, N., Adachi, S., Okumura, H., and Kouyama, T. (2004). Crystal structure of the M intermediate of bacteriorhodopsin: allosteric structural changes mediated by sliding movement of a transmembrane helix. J. Mol. Biol. *341*, 1023–1037.

Tozzini, V. (2005). Coarse-grained models for proteins. Curr. Opin. Struct. Biol. *15*, 144–150.

Vincent, J., Andersson, M., Eklund, M., Wohri, A.B., Odelius, M., Malmerberg, E., Kong, Q., Wulff, M., Neutze, R., and Davidsson, J. (2009). Solvent dependent structural perturbations of chemical reaction intermediates visualized by time-resolved x-ray diffraction. J. Chem. Phys. *130*, 154502.

Vonck, J. (2000). Structure of the bacteriorhodopsin mutant F219L N intermediate revealed by electron crystallography. EMBO J. *19*, 2152–2160.